

Synthesis, structural study, thermal, optical properties and characterization of the new compound $(C_6H_7N_2O_2)_3TeCl_5 \cdot 2Cl$

D. Maraii^a, J. Farjas^b, X. Fontrodona^b, M. Dammak^a

^aLaboratoire de Chimie Inorganique, Faculté des Sciences de Sfax, University of Sfax, BP 1171, 3000 Sfax,
Tunisia

^bUniversity of Girona, Campus Montilivi, Edif. PII, E17071 Girona, Catalonia, Spain

Corresponding author: mariidhaou@hotmail.fr

Abstract

The new organic–inorganic compound, $[(C_6H_7N_2O_2)_3TeCl_5 \cdot 2Cl]$ was synthesized and its structure was determined at room temperature in the triclinic system ($P\bar{1}$) with the following parameters: $a = 10.5330(11)\text{Å}$, $b = 10.6663(11)\text{Å}$, $c = 15.9751(16)\text{Å}$, $\alpha = 82.090(2)^\circ$, $\beta = 71.193(2)^\circ$, $\gamma = 68.284(2)^\circ$ and $Z = 2$. The final cycle of refinement led to $R = 0.057$ and $R_w = 0.149$. The crystal structure was stabilized by an extensive network of N–H...Cl and non-classical C–H...Cl hydrogen bonds between the cation and the anionic group. Several thermal analysis techniques such as thermogravimetric analysis, the differential scanning calorimetric analysis and Evolved Gas Analysis were used. We used isoconversional kinetics methods to determine the kinetics parameters. We observe that the decomposition of $[(C_6H_7N_2O_2)_3TeCl_5 \cdot 2Cl]$ entails the formation hydrochloric acid of nitroaniline as volatiles. The infrared spectra were recorded in the $4000\text{--}400\text{ cm}^{-1}$ frequency region. The Raman spectra were recorded in the external region of the anionic sublattice vibration $50\text{--}1500\text{ cm}^{-1}$. The optical band gap was calculated from the UV–Vis absorbance spectra using classical Tauc relation which was found to be 3.12 and 3.67 eV.

Keywords: Thermal Analysis, Kinetics Parameters, Structural Analysis, FTIR, Raman, Optical absorption.

Introduction

The revolutionary increase in the number of synthesized and structurally characterized coordination polymers in the last few decades reflects the effort devoted to the search for catalytic, conducting, luminescent, magnetic or porous materials [1-2]. Besides, the use of tellurium as a potential node of the metal-organic framework allows a better understanding of the correlations between structural features and physical characteristic [3]. In addition, Te atoms act as a part of the heterometallic inorganic clusters [4-5]. There are several types of interactions, such as the interaction with another metal [6-7] or with halogens [8-9]. Therefore, tellurium-coordination polymers are organic-inorganic hybrid materials with several potential applications [10].

Besides, there is a growing interest in m-Nitroaniline as nitro- substituted derivatives of aromatic amines because aromatic amines are highly toxic and they are suspected of having carcinogenic properties [11]. For instance, 3-Nitroaniline is extensively used to treat wastewater.

3-Nitroaniline contains three nitrogen atoms and three amino substituents and crystallizes as a hydrogen-bonded solid that comprises molecular tapes formed by C–H...N hydrogen bonds between the adjacent molecules. As a result 3-Nitroaniline represents an extremely interesting ligand system for supramolecular chemistry [12-13]. Generally, the solid state complexation of m-Nitroaniline with different organic and inorganic acids comprises mostly the weak hydrogen bonds of N-H...Cl and C-H...Cl types [14-16]. So, the use of 3-Nitroaniline with hexahydrotellurate gives birth to a new $[(C_6H_7N_2O_2)_3TeCl_5 \cdot 2Cl]$ complex. In this paper we report the synthesis of $[(C_6H_7N_2O_2)_3TeCl_5 \cdot 2Cl]$ single crystals. These crystals are characterized by XRD, FTIR and Raman studies. Their stability is characterized by means of thermal analysis.

2. Experimental procedure

2.1. Synthesis of $(C_6H_7N_2O_2)_3TeCl_5 \cdot 2Cl$ compound

$(C_6H_7N_2O_2)_3TeCl_5 \cdot 2Cl$ is obtained from a mixture of $C_6H_6N_2O_2$ (99.98%), $Te(OH)_6$ (98%) that was dissolved in 38% concentrated HCl acid and was stirred for a few minutes at room temperature. After slow evaporation, needles-shaped monocrystals appeared in the solution. The colorless crystals were collected by filtration and washed rapidly with cold ethanol. The stoichiometry of the process is:



2.2.Characterization

2.2.1. X-ray diffraction

The crystal data, collected reflections and parameters of the final refinement are reported in Table 1. Intensity data was collected using a Bruker APEXII CCD four circle diffractometer with graphite monochromated (Mo K α). The positional parameters for the heavy atoms were obtained from a three-dimensional Patterson map, while the non-H atoms were found from successive difference Fourier Maps. The structure is refined by full matrix least squares using anisotropic temperature factors for all non-hydrogen atoms. The H atoms were all located in a difference map, but those attached to carbon atoms were repositioned geometrically. The H atoms were initially refined with soft restraints on the bond lengths and angles to regularize their geometry and $U_{\text{iso}}(\text{H})$ (in the range 1.2–1.5 times U_{eq} of the parent atom), after which the positions were refined with riding constraints. Calculations were performed with the SHELXS [17] and SHELXL [18] programs, using the scattering factors enclosed therein. The structural graph was created with ORTEP [19] and DIAMOND programs [20].

2.2.2 Spectroscopic measurement

Fourier transform infrared (FT-IR) measurements were performed at room temperature on a Perkin–Elmer FT-IR Paragon 1000 PC spectrometer over the 4000–400 cm^{-1} region. Samples were prepared in KBr pellets. As for the Raman scattering spectrum, it was recorded using a T-64000 Raman spectrometer (ISA, JobinYvon) with standard attachments. The beam sources were argon krypton titan-sapphire and semi-conductor lasers. The spectrum was recorded in the range of 50 to 1500 cm^{-1} . The UV–Vis spectral analysis was carried out between 200 and 800 nm using UV–Vis absorption spectrophotometer (T90+UV/Visible).

2.2.3. Thermal analysis

Differential scanning calorimetric (DSC) analysis was performed using a DSC 822 METTLER TOLEDO instrument for temperatures ranging from 300 to 750 K. The samples were heated at a constant rate of 10 K/min^{-1} . A polycrystalline sample of 4.625 mg was placed in an aluminum crucible and the experiments were carried out under a nitrogen flowing atmosphere.

Thermogravimetric (TG) analysis was performed with a Setaram apparatus model, Setsys Evolution 16. The temperature was increased from 300 to 750 K at a constant rate of 10 K/min^{-1} under a nitrogen atmosphere. To improve the signal–noise ratio, after experiments TG

curves were corrected by subtracting a consecutive identical second measurement and by measuring the sample mass at room temperature after the experiment. TG and DSC temperature and tau lag was calibrated from the melting point of indium and aluminum. To calibrate Tau Lag three heating rates were used: 5, 10 and 20 K/min. DSC signal was calibrated from the melting enthalpy of indium.

Evolved Gas Analysis (EGA) was performed by placing the samples in a quartz tube at a pressure of about 10^{-5} mbar. Samples are heated at a constant rate of 5 K/min using an external furnace.

2.2.4 Kinetic analysis

Friedman's isoconversional method [21, 22] and Kissinger method [23] were employed for the computation of the kinetic parameters. Since TG measurements allowed us to obtain an accurate determination of the evolution of the transformation, Friedman's analysis was used to determine the activation energy. Conversely, from the DSC curves it is impossible to determine unambiguously the baseline, so it is not possible to determine the evolution of the transformed fraction accurately enough to apply an isoconversional method. Thus, to perform the kinetic analysis of the DSC data, we used the Kissinger method that is not as accurate as Friedman's method but it allows determining the activation energy solely from the peak temperature.

3. Results and discussion

3.1. Structure description

Single crystal X-ray analysis shows that $[(C_6H_7N_2O_2)_3TeCl_5 \cdot 2Cl]$ compound crystallizes at room temperature in the space group ($P\bar{1}$) with two formula units in the unit cell ($Z=2$). The cell dimensions are: $a=10.5330(11)\text{\AA}$, $b=10.6663(11)\text{\AA}$, $c=15.9751(16)\text{\AA}$, $\alpha=82.090(2)^\circ$, $\beta=71.193(2)^\circ$, $\gamma=68.284(2)^\circ$ and $V=1578.0(3)\text{\AA}^3$. The asymmetric unit of the title compound is depicted in Figure 1 and shows the presence of an anionic entity formed by square pyramid $[TeCl_5]^-$ entities, two isolated chloride ion Cl^- and three independent 3-nitroanilinium $[C_6H_7N_2O_2]^+$.

Five chlorine atoms surround the tellurium atom in the anionic species and form a square-based pyramidal coordination. Indeed, the environment in the tellurium atom is characterized by five Te-Cl bonds whose distances are between 2.327(2) and 2.642(2) \AA . Cl-Te-Cl bond angles fall in the range of $89.55(9)^\circ$ - $178.28(8)^\circ$. The selected bonds and angles are listed in Table 2. The projection of the atomic arrangement of $[(C_6H_7N_2O_2)_3TeCl_5 \cdot 2Cl]$ in

the (ac) plane is shown in Figure 2 and consists of parallel inorganic layers alternated by organic planes; both planes axes are parallel to the (a b) one. The C–N bond lengths vary from 1.456(9) to 1.49(2) Å. C–C bond lengths vary from 1.353(15) to 1.402(17) Å and angles C–C–C, N–C–C, C–N–O are between 114.7(10)° and 126.9(16)°. In the title compound, the entire ring is planar and is built up by the atoms (C1,C2, C3, C4, C5,C6), (C7,C8, C9, C10, C11,C12),(C13,C14, C15, C16, C17,C18).

In the $[(C_6H_7N_2O_2)_3TeCl_5 \cdot 2Cl]$ compound the organic species interact with the inorganic group via N–H...Cl hydrogen bonds, as shown in Table 3 and in Figure 3. Actually, there are six strong (3.089(7) and 3.184(7) Å) and four weak (3.279(6) and 3.581(7) Å) N–H...Cl hydrogen bonds [24]. The intermolecular hydrogen bonding contacts C–H...Cl provide a linkage between the $(C_6H_7N_2O_2)^+$ entities and the $[TeCl_5]^-$ anions (3.585(8)-3.646(9)Å).

3.2. Thermal Analysis

The evolution of the mass (TG signal) when the sample is submitted to a constant temperature rise is shown in Figure. 4. The sample is stable up to 130°C. The decomposition is triggered by an endothermic process. This endothermic process is not a melting or evaporation because it is thermally activated; the process shifts to higher temperature when the heating rate is increased [25]. Besides, the analysis of the morphology of the solid sample at 150°C does not reveal any melting process.

In Figure 4.b, we have plotted the evolution of the time derivative of the TG signal (DTG) together with the DSC signal. Both parameters are directly related to the transformation rate and they allow an easier identification of the different stages of the decomposition process. Three decomposition stages can be clearly distinguished, the first of which is endothermic and appears as a shoulder in the DTG signal. As for the second stage, it is located around 200°C and involves the larger mass loss. This stage is an exothermic process. Concerning the third stage, it is located approximately between 250 and 300°C and is also an exothermic process. After the decomposition, the mass continues to decrease steadily because the final decomposition product is not stable. Indeed, the mass decreases up to 900°C where no solid product is left.

3.3. Kinetic analysis

In this section we perform a kinetic analysis to determine the activation energy. Isoconversional methods allow the determination of the kinetic parameters without assuming any particular reaction mechanism, i.e., they are model-free. They are based on the determination of one or more of the system parameters (temperature, transformation rate...) at

which the same degree of transformation, α , has been reached for the measurements performed at different constant temperatures (isothermal) or different heating rates (non-isothermal). In general, non-isothermal experiments are preferred [26] because they are easier and faster to perform and can explore a wider temperature range. Isoconversional methods rely on the hypothesis that at a given α , the transformation rate is only a function of temperature [26,27],

$$\left[\frac{d \ln(d\alpha / dt)}{dT^{-1}} \right]_{\alpha} = -\frac{E_{\alpha}}{R} \quad (1)$$

Where the subscript α indicates the degree of transformation, R is the gas constant, and E_{α} is the activation energy. The integration of Eq. (1) results in a transformation governed by a single mechanism where the rate constant, $k_{\alpha}(T) = A_{\alpha} \exp(-E_{\alpha} / RT)$, depends on α [28]:

$$\frac{d\alpha}{dt} = A_{\alpha} \exp\left[-\frac{E_{\alpha}}{RT}\right] f(\alpha) \quad (2)$$

A variation of E_{α} with α is usually related to the occurrence of complex transformations where several mechanisms are involved (such as heterogeneous transformations, multi-step reactions, or transformations depending on parameters other than α and T) [29–32]. In this context, Eq. (1) is an approximate relationship and E_{α} must be interpreted in terms of apparent activation energy.

In Fig. 5, we have plotted the evolution of the transformation which was obtained directly from the TG analysis (Fig. 4). To calculate the degree of transformation, we have assumed that α depends linearly on the mass evolution:

$$\alpha(t) = \frac{m_{in} - m(t)}{m_{in} - m_{fin}} \quad (3)$$

Where m_{in} and m_{fin} are the initial and final masses, respectively.

To determine the activation energy, we have used the Friedman method [21] which is an accurate and reliable method [22,32]. The result is plotted in Fig 6. From Fig. 6 it is apparent that the activation energy is not constant, this complex behavior is related to the overlapping of different processes. Indeed, from Fig. 5, it is clear that at least three different mechanisms are involved in the decomposition process. Since from Fig. 5 three DSC peaks can be clearly distinguished, we also perform the Kissinger analysis [23] which is based on the determination of the peak temperature, T_M . The peak temperature is the temperature at which the transformation rate is at its maximum. If we assume that, within the range where a

peak is observed, the transformation is ruled by a single mechanism, the transformation rate is described by single process equation [33,34]:

$$\frac{d\alpha}{dt} = A \exp(-E / RT) \quad (4)$$

Contrarily to Eq. (2), E and A are assumed constant, they do not depend on α . From Eq. (4) one can easily derive the Kissinger equation [34] that relates the peak temperature, T_M , with the kinetic parameters:

$$\ln\left(\frac{\beta}{T_M^2}\right) = -\frac{E}{RT_M} + \ln\left(-\frac{AR}{E} f'(\alpha_M)\right) \quad (5)$$

Where β is the heating rate, $f'(\alpha_M) \equiv df/d\alpha|_{\alpha=\alpha_M}$ and α_M is the degree of transformation at T_M .

Eq. (5) has been used to determine the activation energy for a large variety of transformations [35–42]. Kissinger method relies on the determination of the peak temperature $T_{M,i}$ from experiments carried out at different heating rates β_i . The activation energy is obtained from a linear fit of the plot $\ln(\beta_i / T_{M,i}^2)$ versus $1/T_{M,i}$. The results are plotted in Fig. 7 for the three DSC peaks observed in Fig. 4.

The Kissinger analysis reveals that the endothermic process that triggers the decomposition exhibits a quite high energy barrier, 168 kJ/mol. Conversely, the Friedman analysis delivers significantly smaller activation energy. The reason is that the first process involves a very low mass loss as it is apparent from Fig. 4. For instance, the DTG curve shows only a small shoulder. Therefore, this process is not caught by the Friedman analysis that is based on the TG signal. On the other hand, the process is more evident in the DSC signal, thus Kissinger analysis of the first DSC peak is able to disclose the value of this initial barrier.

The Kissinger analysis of the second peak that is related to the second stage delivers an activation energy of 109 kJ/mol. This second stage covers most of the decomposition process. Friedman analysis reveals a roughly constant activation energy of around 125 kJ/mol for $0.25 < \alpha < 0.7$. This discrepancy could be partly attributed to the experimental uncertainties in the determination of α and to the fact that E_a shows an evolution that points out that the kinetics of this second stage could not be reduced to a single mechanism description. From Figures 4.b and 5, it can be noted that the DTG, DSC and da/dt curves show a structure that is characteristic of the occurrence of a complex behavior.

Finally, the Kissinger plot deviates significantly from linearity in the third process. As can be seen from Fig. 4, the DSC peaks obtained at 10 and 20 K/min nearly overlap and are far away from the peak obtained at 5 K/min. This behavior is in contradiction with the expected separation between the peaks for thermally activated process [22]. The use of the Arrhenius equation to describe the reaction kinetics is based on the assumption that the reaction takes place in a parameter region far from equilibrium. The deviations from the Arrhenius behavior are to be expected when reactions take place near equilibrium. In these cases, the transformation rate is also governed by the temperature difference with respect to the equilibrium temperature. Indeed, when the temperature approaches that of equilibrium, the processes obtained at different heating rates tend to overlap. Therefore, the non-linearity of Kissinger plot may be interpreted in terms of a reaction kinetics controlled by the separation from equilibrium. In the Friedman plot, we observe an anomalous and very low activation energy. The latter also indicates that the assumption that the reaction rate is governed by Arrhenius dependence does not hold.

3.4. EGA analysis

The main volatiles identified by EGA when $[C_6H_7N_2O_2]_3TeCl_5 \cdot 2Cl$ is heated at a rate of 5K/min are shown in Figure 8. In Figure 8 only the evolution of the main fragments is exhibited, but volatile identification is based on the complete analysis of the defragmentation pattern. The first and main volatile is hydrochloric acid, so the decomposition of $[C_6H_7N_2O_2]_3TeCl_5 \cdot 2Cl$ is probably triggered by the release of the two chloride atoms. Next, we observe the formation of nitroaniline $C_6H_4(NH_2)(NO_2)$. Therefore, the released chlorine atoms may react with $[C_6H_7N_2O_2]_3TeCl_5$ to form $C_6H_4(NH_2)(NO_2)$, $TeCl_5$ and $2HCl$. The stoichiometry of the process is:



The final solid residue is $TeCl_5$ which is known to be a volatile, because the components of the form MX_n with $n = 1, 2, \dots$; $M = Te, P, Cu \dots$ and $X = Cl, Br, I, F \dots$ have boiling points around 150 to 300°C for example the boiling point of $SeBr_6$ is 180 °C [43]. So the final steady mass evolution after decomposition up to a null residue (zero final mass) is probably due to the evaporation of $TeCl_5$.

The formation of small amounts of H_2O is probably related to the reaction of HCl with residual O_2 . As for the formation of CO_2 at higher temperature, it is probably related to the decomposition of nitroaniline in the gas phase.

3.5. Infrared and Raman spectroscopy

The IR spectrum of this compound, Figure 9 and Table 4 shows the characteristic absorption peaks of the $[\text{C}_6\text{H}_7\text{N}_2\text{O}_2]^+$ cation, which were described in refs. [44, 45]. The peaks at 3426 cm^{-1} correspond to the (N-H) stretching vibrations. The symmetric stretching vibrations of (C-H) are observed at 3071 cm^{-1} . The bands observed between 2850 and 2569 cm^{-1} are assigned to the asymmetric stretching vibrations of the (C-H). The (N-H) bending is observed at 1614 cm^{-1} . The symmetric and asymmetric stretching vibrations of (NO_2) are observed at 1344 and 1528 cm^{-1} . The (C-C-H) bending mode is located at 1087 cm^{-1} . The vibrations modes between 891 and 806 cm^{-1} are due to the (C-N) asymmetric and symmetric stretching vibrations. The deformation of (C-C) is observed at 720 and at 488 cm^{-1} , respectively.

The Raman spectrum is illustrated in Fig. 10 and Table 6. In comparison with previous research works reported on similar compounds containing $[\text{TeCl}_5]$ [46, 47], the asymmetric stretching of (NO_2) and the deformation of (C-H) are observed at 1355 and at 1214 cm^{-1} , respectively. Besides, the band located at 806 cm^{-1} is caused by the symmetric stretching of the (C-N). The observed bands at 673 cm^{-1} are associated with the (NO_2) rocking mode.

The bands corresponding to the (Te-Cl) stretching in-plane mode appear at 340 cm^{-1} . The stretching modes of (Te-Cl) occur between 265 - 311 cm^{-1} and the deformation out-of-plane of (TeCl_5) modes can be observed between 65 and 108 cm^{-1} .

3.6. Optical study

The optical properties of solids provide an important tool for studying energy band structure. The optical absorption spectrum shown in Fig. 11 indicates that there is a strong absorption at 338 and 397 nm . This may be due to nitrogen-containing aromatic systems or electronic excitation in this region [48, 49]. Essentially, a high energy raises the electrons to higher bands, so the crystal structure absorbs the light, while the light without enough energy to raise the electrons to the following band will pass through the structure. The optical energy band gap for the $[(\text{C}_6\text{H}_7\text{N}_2\text{O}_2)_3\text{TeCl}_5 \cdot 2\text{Cl}]$ crystal was calculated by classical Tauc relation [50, 51] as given below:

$$\alpha h\nu = A(h\nu - E_g)^n \quad (7)$$

Where A is a constant, $h\nu$ is the photon energy, E_g is the energy band gap, α is the absorption coefficient given by $\alpha = 2.303(A_b / t)$, where A_b is the absorbance and t is the thickness of cuvette which is 0.5 cm in the present case. The value of $n=1/2, 3/2, 2,$ or 3 depending on the nature of the electronic transition responsible for absorption. The value of $n=1/2$ allows for

the direct transition, thereby giving direct band gap. The direct optical band gap of the crystal has also been determined by plotting $(\alpha h\nu)^2$ against the photon energy ($h\nu$).

Fig. 12 shows the plot of $(\alpha h\nu)^2$ vs. photon energy ($h\nu$) for the $[(C_6H_7N_2O_2)_3TeCl_5 \cdot 2Cl]$ crystal. The optical energy gap E_g is determined from the intersection of the extrapolated line with the photon energy axis at ($\alpha=0$). The direct optical band gap of the crystal is found to be 3.12 and 3.67 eV. As a consequence of this wide band gap, the grown crystal has a large transmittance in the visible region. The large transmission in the entire visible region enables it to be a good candidate for electro-optic applications [52].

4. Conclusions

$[(C_6H_7N_2O_2)_3TeCl_5 \cdot 2Cl]$ single-crystals have been grown by the slow evaporation method. $[(C_6H_7N_2O_2)_3TeCl_5 \cdot 2Cl]$ crystallizes in the space group P-1 with triclinic system. The crystal structure is stabilized by the various types of N-H ... Cl and C-H ... Cl hydrogen bonds.

The TGA and DSC study shows that the compound is stable up to 130°C; thermal analysis reveals the existence of three decomposition stages at 130, 200 and between 250-300 °C.

The kinetic analysis reveals that the decomposition is a complex transformation that involves several processes and that the decomposition is triggered by an endothermic process whose barrier the activation energy is 168 kJ/mol.

From Evolved Gas Analysis we observed that the decomposition is triggered by the release of two chloride atoms and that the decomposition entails the formation of hydrochloric acid and nitroaniline as volatiles.

The presence of all the fundamental functional groups of the grown sample was confirmed by Raman scattering and infrared spectroscopy.

From UV-visible spectrum, the cut-off wavelength and optical band gap were (397 nm) 3.12 eV and (338 nm) 3.67 eV.

Acknowledgements

This work was partially funded by the Tunisian Ministry of Higher Education and Scientific Research, the Spanish Programa Nacional de Materiales through project MAT2014-51778-C2-2-R and by the Universitat de Girona contract No. MPCUdG2016/059.D. Maraii

acknowledges the financial support of the Tunisian Ministry of Higher Education and Scientific Research.

Appendix A. Supplementary data

CCDC 1025391 contains the supplementary crystallographic data for this paper. These data can be obtained free of charge via [http:// www.ccdc.cam.ac.uk/conts/retrieving.html](http://www.ccdc.cam.ac.uk/conts/retrieving.html), or from the Cambridge Crystallographic Data Centre, 12 Union Road, Cambridge CB2 1EZ, UK; fax: (+44) 1223 336 033; or e-mail: deposit@ccdc.cam.ac.uk.

References

- [1] B. Moulton, M.J. Zaworotko, From Molecules to Crystal Engineering: Supramolecular Isomerism and Polymorphism in Network Solids, *Chem. Rev.* 101 (2001) 1629-1658.
- [2] S. Kitagawa, R. Kitaura, S. Noro, Functional Porous Coordination Polymers, *Angew. Chem. Int. Ed.* 43 (2004) 2334-2375.
- [3] M. Dammak, T. Mhiri, J. Jaud, J.M. Savariault, Structural study of the two new caesium sulfate and selenatetellurate $Cs_2SO_4 \cdot Te(OH)_6$ and $Cs_2SeO_4 \cdot Te(OH)_6$ *J. Inorg. Mater.* 3 (2001) 861-873.
- [4] K.A. Brylev, Y.V. Mironov, N.G. Naumov, V.E. Fedorov, New Compounds from Tellurocyanide Rhenium Cluster Anions and 3d-Transition Metal Cations Coordinated with Ethylenediamine, J.A. Ibers, *Inorg. Chem.* 43 (2004) 4833-4838.
- [5] S.B. Artemkina, N.G. Naumov, A.V. Virovets, V.E. Fedorov, 3D-Coordination Cluster Polymers $[Ln(H_2O)_3Re_6Te_8(CN)_6] \cdot nH_2O$ ($Ln = La^{3+}, Nd^{3+}$): Direct Structural Analogy with the Mononuclear $LnM(CN)_6 \cdot nH_2O$ Family, *Eur. J. Inorg. Chem.* (2005) 142-146.
- [6] M. Bochmann, A.P. Coleman, K.J. Webb, M.B. Hursthouse, M. Mazid, Synthesis of Sterically Hindered Tellurophenols and the Structure of $[Cd(\mu\text{-}TeC_6H_2M_3)_2]_{\infty}$ *Angew. Chem. Int. Ed.* 30 (1991) 973-975.
- [7] J. Lee, D. Freedman, Trivalent Lanthanide Chalcogenolates: $Ln(SePh)_3$, $Ln_2(EPh)_6$, $Ln_4(SPh)_{12}$, and $[Ln(EPh)_3]_n$ ($E = S, Se$). How Metal, Chalcogen, and Solvent Influence Structure, *J. Inorg. Chem.* 37 (1998) 2512-2519.
- [8] P.H. Bird, V. Kumar, B.C. Pant, Crystal and Molecular Structures of the (4-alkoxyphenyl)tellurium (IV) Trihalides: $(4\text{-EtOPh})TeCl_3$, $(4\text{-EtOPh})TeBr_3$, and $(4\text{-MeOPh})TeI_3$, *Inorg. Chem.* 19 (1980) 2487-2493.
- [9] N.W. Alcock, W.D. Harrison, Structure of *catena*- μ -bromo-dibromo(phenyl)-tellurium(IV), *Acta Crystallogr. B* 38 (1982) 2677-2679.

- [10] C. Janiak, Engineering coordination polymers towards applications, Dalton Trans. (2003) 2781-2804.
- [11] Dimou, A.D., Sakkas, V.A., Albanis, T.A. Photodegradation of trifluralin in natural waters and soils: degradation kinetics and influence of organic matter. Int. J. Environ. Anal.Chem. 84(2004) 173.
- [12] N. Singh, A. Ahmad, Synthesis and spectrophotometric studies of charge transfer complexes of p-nitroaniline with benzoic acid in different polar solvents, Journal of Molecular Structure 1074 (2014) 408-415.
- [13] N. Wang and al. N. Wang and al. Chemical Engineering Journal 260 (2015) 386,Chemical Engineering Journal 260 (2015) 386-392.
- [14] J.A. Zerkowski, J.C. McDonald, G.M. Whitesides, Investigations into the Robustness of Secondary and Tertiary Architecture of Hydrogen-Bonded Crystalline Tapes , Chem. Mater. 6 (1994) 1250-1257.
- [15] J. Janczak, G.J. Perpetuo, Melaminium chloride hemihydrate, ActaCrystallogr. C57 (2001) 1120-1122.
- [16] M. Ratajczak-Sitarz, Z. Kałuski, A. Ostrowicz, S. Bałoniak, Molecular and Crystal Structure of 3-(4-Chlorophenylthio)-1-(2,4-Dinitrophenylamino)-Pyrrolidine-2,5-Dione , J. Crystallogr. Spectrosc. Res. 20 (1990) 535-539.
- [17] G.M. Sheldrick, Program for the Crystal Structure Determination; SHELXS-97, (1990).
- [18] G.M. Sheldrick, Program for the Crystal Structure Determination; SHELXL-97, (1997).
- [19] L.J. Farrugia, ORTEP-3 for Windows - a version of ORTEP-III with a Graphical User Interface (GUI), J. ApplCryst. 30 (1997) 565.
- [20] K. Brandenburg, Diamond Version2.0 Impact Gbr, Bonn, Germany, 1998.
- [21] H.L. Friedman, Kinetics of thermal degradation of char-forming plastics from thermogravimetry. Application to a phenolic plastic, J. Polym.Sci. Part C Polym.Symp. 6 (1964) 183–195.
- [22] J. Farjas, P. Roura, Isoconversional analysis of solid state transformations. A critical review.Part I. Single step transformations with constant activation energy, J. Therm. Anal.Calorim. 105 (2011) 757–766.
- [23] H.E. Kissinger, Reaction Kinetics in Differential Thermal Analysis, Anal. Chem. 29 (1957) 1702–1706.
- [24] G.C. Pimental, A.L. Mc Clellan, The Hydrogen Bond, Freeman, San Fransisco, 1971.

- [25] J. Farjas, P. Roura, Exact analytical solution for the Kissinger equation: Determination of the peak temperature and general properties of thermally activated transformations, *Thermochim. Acta.* 598 (2014) 51–58.
- [26] S. Vyazovkin, C.A. Wight, Isothermal and Nonisothermal Reaction Kinetics in Solids: In Search of Ways toward Consensus, *J. Phys. Chem. A.* 101 (1997) 8279–8284.
- [27] S. Vyazovkin, Thermal analysis., *Anal. Chem.* 82 (2010) 4936–49.
- [28] J. Farjas, P. Roura, Isoconversional analysis of solid-state transformations. A critical review. Part III. Isothermal and non isothermal predictions, *J. Therm. Anal. Calorim.* 109 (2012) 183–191.
- [29] S. Vyazovkin, C.A. Wight, Kinetics in solids., *Annu. Rev. Phys. Chem.* 48 (1997) 125–49.
- [30] S. Vyazovkin, On the phenomenon of variable activation energy for condensed phase reactions, *New J. Chem.* 24 (2000) 913–917.
- [31] F. Wilburn, Kinetics of overlapping reactions, *Thermochim. Acta.* 354 (2000) 99–105.
- [32] J. Farjas, P. Roura, Isoconversional analysis of solid state transformations. A critical review. Part II. Complex transformations, *J. Therm. Anal. Calorim.* 105 (2011) 767–773.
- [33] M. Brown, D. Dollimore, A. Galwey, Theory of Solid State Reaction Kinetics, in: C.H. Bamford, C.F.H. Tipper (Eds.), *Compr. Chem. Kinet. Vol 22, React. Solid State*, Elsevier, Amsterdam, 1980: pp. 41–113.
- [34] J. Šesták, Thermophysical properties of solids, their measurements and theoretical analysis, Elsevier, Amsterdam, 1984.
- [35] J. Farjas, P. Roura, Modification of the Kolmogorov–Johnson–Mehl–Avrami rate equation for non-isothermal experiments and its analytical solution, *Acta Mater.* 54 (2006) 5573–5579.
- [36] R.L. Blaine, H.E. Kissinger, Homer Kissinger and the Kissinger equation, *Thermochim. Acta.* 540 (2012) 1–6.
- [37] S. Vyazovkin, A.K. Burnham, J.M. Criado, L.A. Pérez-maqueda, C. Popescu, N. Sbirrazzuoli, ICTAC Kinetics Committee recommendations for performing kinetic computations on thermal analysis data, *Thermochim. Acta.* 520 (2011) 1–19.
- [38] A. Khawam, D.R. Flanagan, Basics and applications of solid-state kinetics: a pharmaceutical perspective., *J. Pharm. Sci.* 95 (2006) 472–98.
- [39] E.J. Mittemeijer, Analysis of the kinetics of phase transformations, *J. Mater. Sci.* 27 (1992) 3977–3987. doi:10.1007/BF01105093.

- [40] M.J. Starink, On the applicability of isoconversion methods for obtaining the activation energy of reactions within a temperature-dependent equilibrium state, *J. Mater. Sci.* 32 (1997) 6505–6512.
- [41] T. Ozawa, Thermal analysis — review and prospect, *Thermochim.Acta.* 355 (2000) 35–42.
- [42] J.P. Elder, The general applicability of the Kissinger equation in thermal analysis, *J. Therm. Anal.* 30 (1985) 657–669.
- [43] O. Reich S. Hasche, K. Büscher, I. Beckmann and B. Krebs, Neue Oxonium-Bromochalkogenate(IV) — Darstellung, Struktur und Eigenschaften von $[\text{H}_3\text{O}][\text{TeBr}_5] \cdot 3\text{C}_4\text{H}_8\text{O}_2$ und $[\text{H}_3\text{O}]_2[\text{SeBr}_6]$, *Z. anorg. allg. Chem.* 622 (1996) 1011-1018.
- [44] V. Krishnakumar, R. Nagalakshmi, Studies on the first-order hyperpolarizability and terahertz generation in 3-nitroaniline, *Physica B* 403 (2008) 1863-1869.
- [45] M. Karabacak, Etem Kose, and Ahmet Atac, Molecular structure (monomeric and dimeric structure) and HOMO–LUMO analysis of 2-aminonicotinic acid: A comparison of calculated spectroscopic properties with FT-IR and UV–vis, *Spectrochimica Acta Part A* 91 (2012) 83-96.
- [46] J. Pietikainen and al, Halogenation of tellurium by SO_2Cl_2 . Formation and crystal structures of $(\text{H}_3\text{O})[\text{Te}_3\text{Cl}_{13}] \cdot 1/2\text{SO}_2$, $[(\text{C}_4\text{H}_8\text{O})_2\text{H}][\text{TeCl}_5] \cdot (\text{C}_4\text{H}_8\text{O})$, $[(\text{Me}_2\text{SO})_2\text{H}] 2[\text{TeCl}_6]$, and $[\text{Ni}(\text{NCCH}_3)_6][\text{Te}_2\text{Cl}_{10}]$, *Polyhedron* 21 (2002) 1089-1095.
- [47] J. B. Milnee, E. J. Gabe, and C. Bensimon. Can. The structure of the tetrachlorohydroxotellurate(IV) anion in $\text{KTeC}_{14}(\text{OH}) \cdot 0.5\text{H}_2\text{O}$ and $\text{KTeC}_{14}(\text{OH})$, *J. Chem.* 69 (1991) 648-652.
- [48] K. Jarraya, N. Gublin, N. Guermani, T. Mhiri, Decomposition behavior of the $\text{NaH}_2(\text{PO}_4)0.48(\text{AsO}_4) 0.52\text{H}_2\text{O}$ compound above room temperature shown by the study of Raman X- ray powder and ac-conductivity, *J. Mater. Sci. Eng.* 28 (2012) 012046.
- [49] V. Sangeetha, K. Gayathri, P. Krishnan, N. Sivakumar, N. Kanagathara and G. Anbalagan, Growth, optical, thermal, dielectric and microhardness characterizations of melaminiumbis (trifluoroacetate) trihydrate single crystal, *J. Crystal Growth* 389 (2014) 30-38. et al, Growth, optical, thermal, dielectric and microhardness characterizations of melaminiumbis (trifluoroacetate) trihydrate single crystal, *J. Crystal Growth* 389 (2014) 30-38.
- [50] J. Tauc, *Amorphous and Liquid Semiconductors*, Plenum, London, (1974) 171.
- [51] J. Tauc, R. Grigorovici, A. Vancu, *Optical Properties and Electronic Structure of Amorphous Germanium*, *Phys. Status Solidi b* 15 (1996) 627-637.

[52] P. Rajesh, P. Ramasamy, Growth of dl-malic acid-doped ammonium dihydrogen phosphate crystal and its characterization, J. Cryst. Growth 311 (2009) 3491-3497.

Tables captions

Table 1: Experimental data for X-ray diffraction study of $[(C_6H_7N_2O_2)_3TeCl_5 \cdot 2Cl]$.

Table 2: Main distances (\AA) and bond angles ($^\circ$) in the $[(C_6H_7N_2O_2)_3TeCl_5 \cdot 2Cl]$ crystal.

Table 3: Main interatomic distances (\AA) and bond angles ($^\circ$) involved in hydrogen bonds.

Table 4: Observed IR and Raman frequencies of $[(C_6H_7N_2O_2)_3TeCl_5 \cdot 2Cl]$ crystal and their assignments.

Figures captions

Fig 1: The asymmetric unit of $(C_3H_7N_2O_2)_3TeCl_5 \cdot 2Cl$ showing the atom-labeling scheme.

Fig.2: Projections of the crystal structure of the title compound view along b direction.

Fig.3: Dotted lines: the intermolecular hydrogen bonds contacts of the title compound.

Fig.4: Simultaneous TG-DSC evolution of $[C_6H_7N_2O_2]_3TeCl_5 \cdot 2Cl$ when the sample is submitted to a continuous heating ramp at different heating rates under N_2 atmosphere: (a) TG-DSC signal, (b) DTG-DSC signal. The sample mass and the DSC signals are normalized to the initial sample mass.

Fig.5: Evolution of the transformed fraction and the transformation rate for the thermal decomposition of $[C_6H_7N_2O_2]_3TeCl_5 \cdot 2Cl$ measured by TG (Fig. 4) at several heating rates.

Fig.6: Friedman analysis of the evolutions shown in Fig 5.

Fig.7: Kissinger plot of the three DSC peaks shown in Fig. 4.

Fig.8: EGA analysis of $[C_6H_7N_2O_2]_3TeCl_5 \cdot 2Cl$ when is submitted to a constant temperature rise of 5 K/min in vacuum (10^{-5} mbar).

Fig.9: Measured IR spectra of the title compound in the region $400-4000\text{ cm}^{-1}$.

Fig.10: Raman spectra of the title compound measured at room temperature in the regions (a) $50 - 1500\text{ cm}^{-1}$.

Fig.11: UV-vis absorbance of the $(C_3H_7N_2O_2)_3TeCl_5 \cdot 2Cl$ crystal.

Fig.12: Plot of $(ah\nu)^2$ versus $(h\nu)$ of the $(C_3H_7N_2O_2)_3TeCl_5 \cdot 2Cl$ crystal.

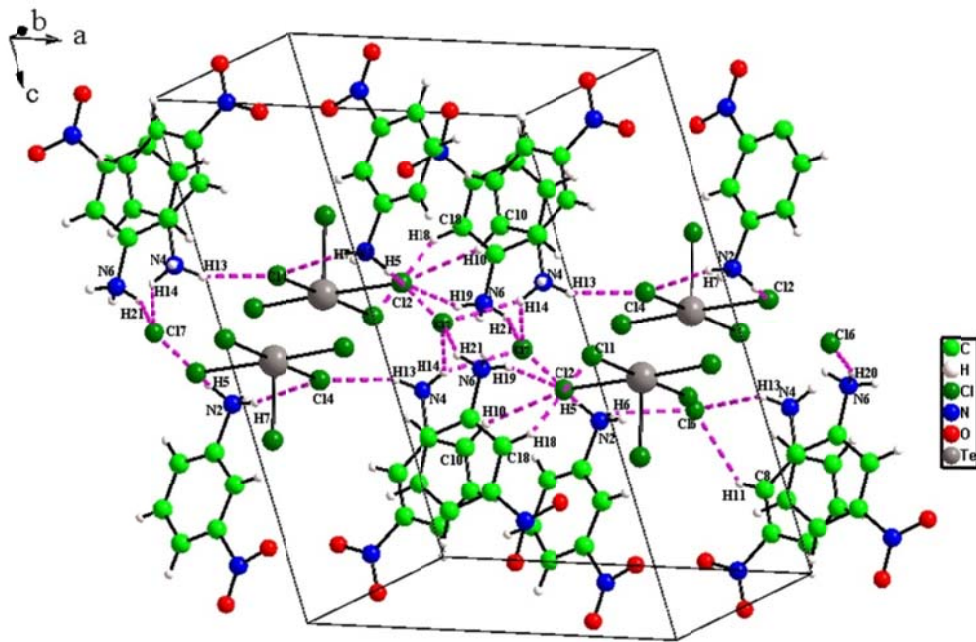


Fig. 3

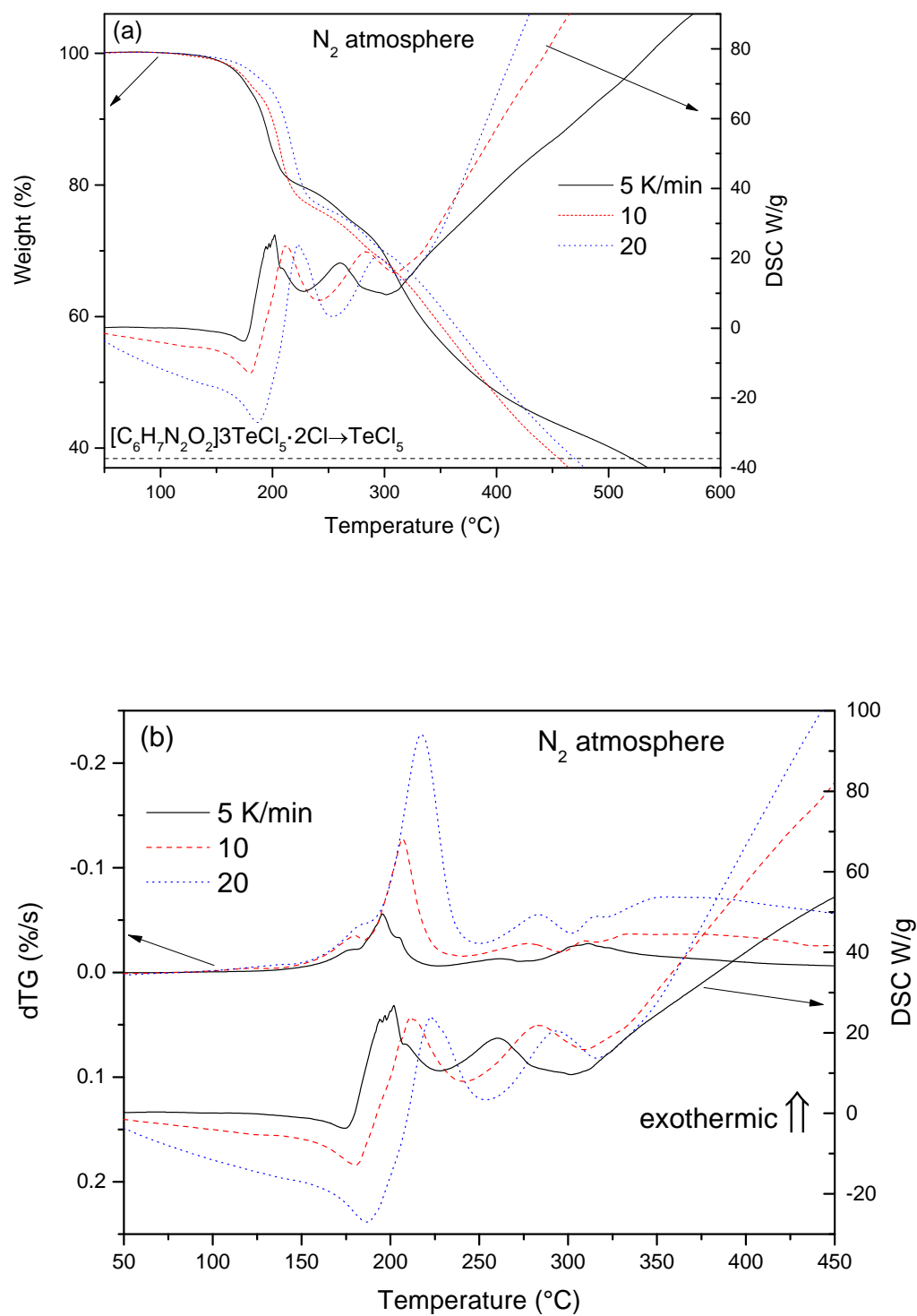


Fig. 4

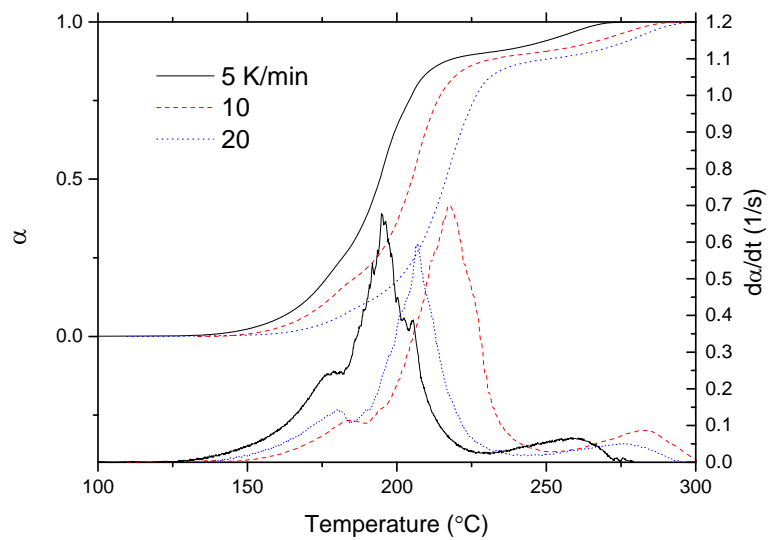


Fig. 5

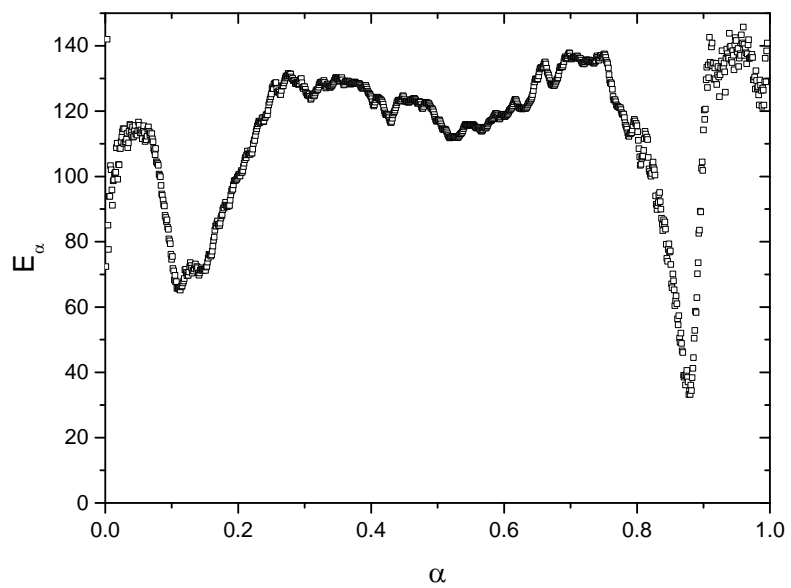


Fig. 6

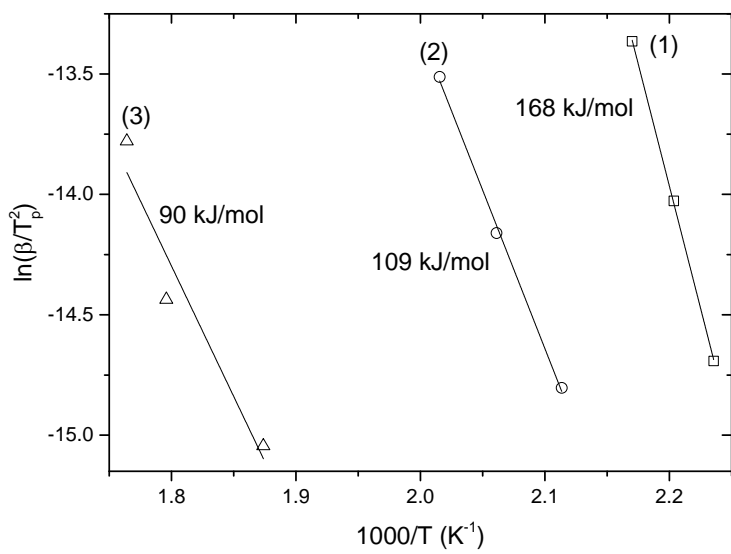


Fig. 7

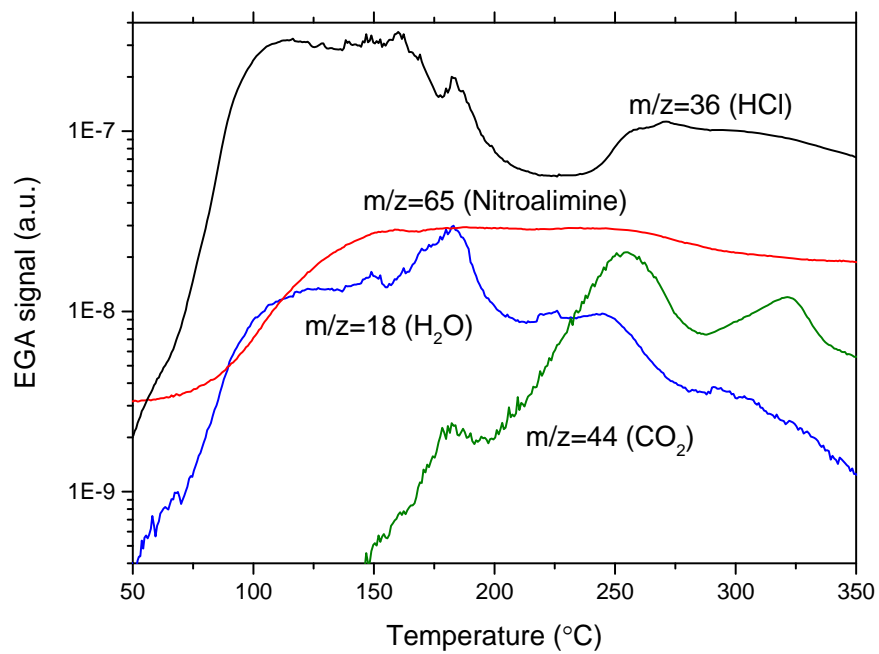


Fig.8

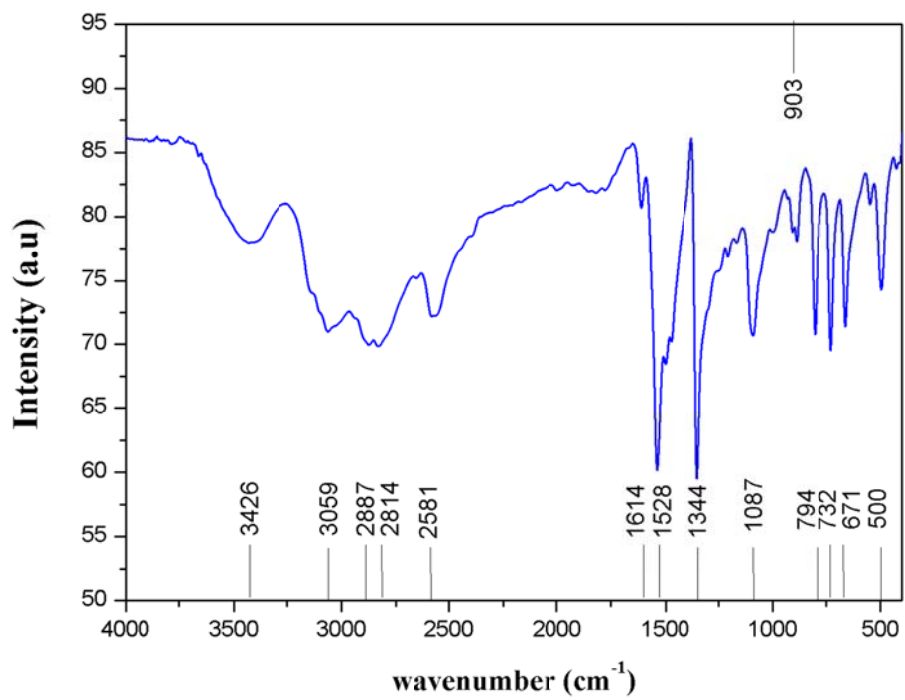


Fig. 9

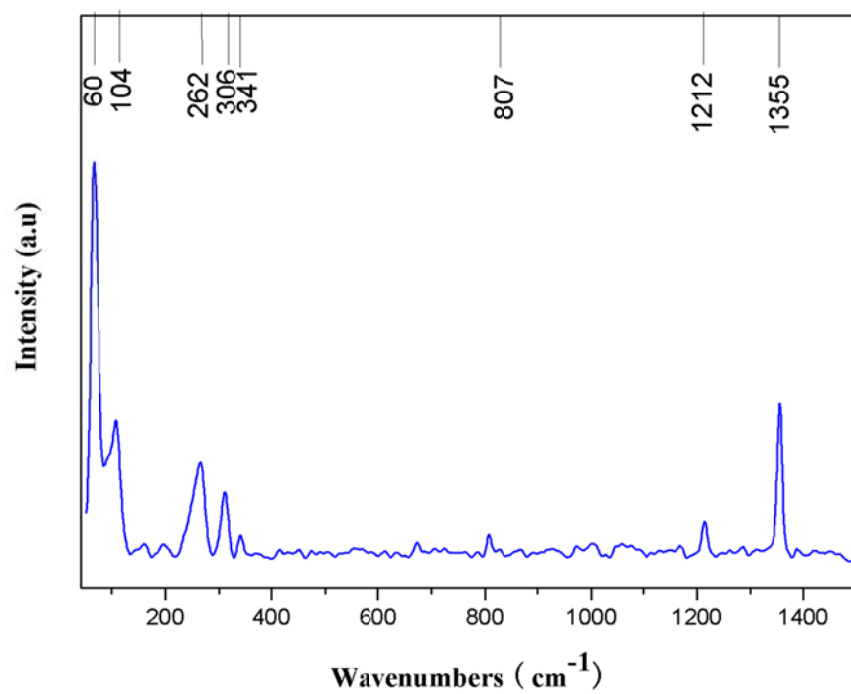


Fig. 10

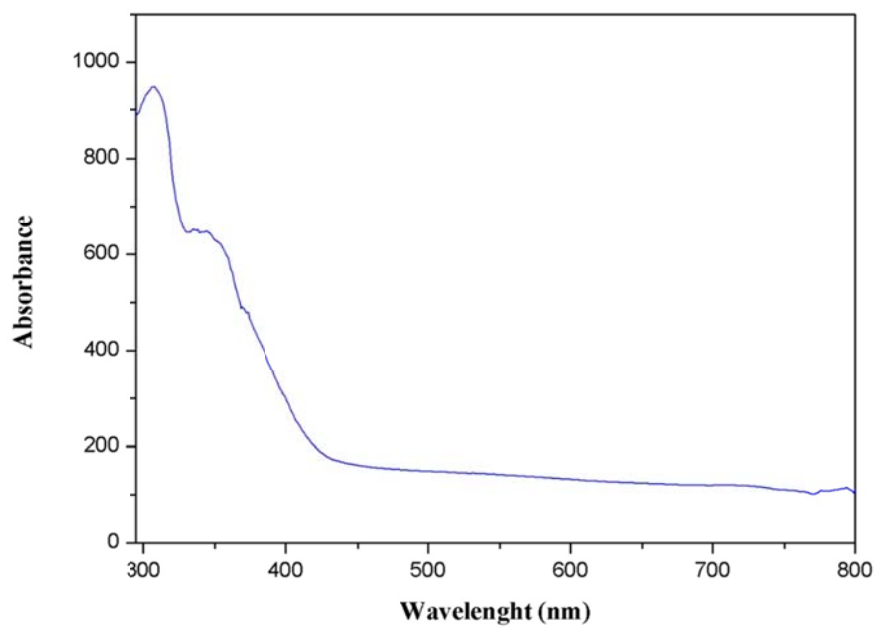


Fig. 11

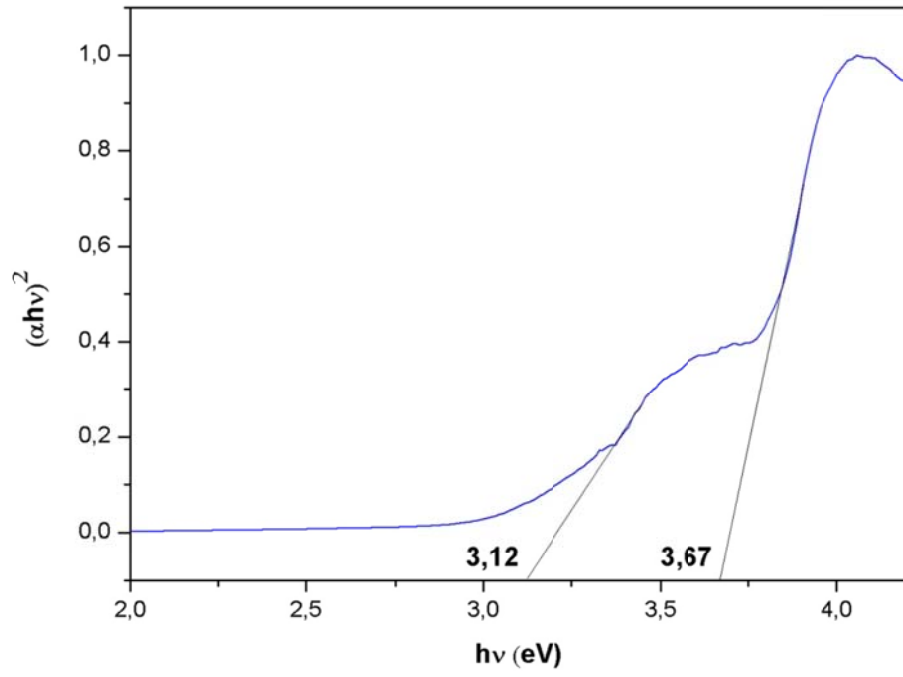


Fig. 12